

Decomposition of the mean friction drag on a NACA4412 airfoil under uniform blowing/suction

Yitong Fan¹, Marco Atzori², Ricardo Vinuesa², Davide Gatti³, Philipp Schlatter², and Weipeng Li^{1*}

¹ School of Aeronautics and Astronautics, Shanghai Jiao Tong University, Shanghai, China, 200240

² SimEx/FLOW, Engineering Mechanics, KTH Royal Institute of Technology, Stockholm, Sweden, SE-100 44

³ Institute of Fluid Mechanics, Karlsruhe Institute of Technology (KIT), Karlsruhe, Germany, D-76131

Abstract

The application of drag-control strategies on canonical wall-bounded turbulence, such as periodic channel and zero- or adverse-pressure-gradient boundary layers, raises the question of how to describe control effects consistently for different reference cases. We employ the RD identity (Renard & Deck, *J. Fluid Mech.*, **790**, 2016, pp. 339–367) to decompose the mean friction drag and investigate the control effects of uniform blowing and suction applied to a NACA4412 airfoil at chord Reynolds numbers $Re_c=200,000$ and $400,000$. The connection of the drag reduction/increase by using blowing/suction with the turbulence statistics (including viscous dissipation, turbulence-kinetic-energy production, and spatial growth of the flow) across the boundary layer, subjected to adverse or favorable pressure gradients, are examined. We found that the peaks of the statistics associated with the friction-drag generation exhibit good scaling in either inner or outer units throughout the boundary layer. They are also independent of the Reynolds number, control scheme, and intensity of the blowing/suction. The small- and large-scale structures are separated with an adaptive scale-decomposition method, *i.e.* empirical mode decomposition (EMD), aiming to analyze the scale-specific contribution of turbulent motions to friction-drag generation. Results unveil that blowing on the suction side of the airfoil is able to enhance the contribution of large-scale motions and to suppress that of small-scales; on the other hand, suction behaves contrarily. The contributions related to cross-scale interactions remain almost unchanged with different control strategies.

Key words: turbulent flows, turbulent boundary layers, turbulence control

1 Introduction

The friction drag (mostly associated with turbulent boundary layers) accounts for approximately 50% of the total aerodynamic drag in long-range commercial aircraft (Gad-el Hak, 1994). It provides great potential for drag reduction and energy saving. Among diverse control strategies for turbulent boundary layers, such as addition of long-chain polymers, oscillating walls, superhydrophobic surfaces, and riblets (White and Mungal, 2008; Toubert and Leschziner, 2012; Rastegari and Akhavan, 2015; Li, 2020; Ran et al., 2021), mass blowing and suction is a promising method to control the friction drag or flow transition in wall-bounded turbulence (Kim et al., 2002; Kametani and Fukagata, 2011).

Experiments have shown that uniform blowing from smooth perforated surfaces can reduce the turbulent friction drag with net-energy saving (Hwang, 1996, 2004). Given the proper blowing intensity, porosity, and effective roughness, the net-energy saving holds for a wide range of conditions, including both zero- and adverse-pressure-gradient (ZPG and APG) turbulent boundary layers (TBLs) (Welch et al., 2001). On the other hand, uniform suction will increase the turbulent friction drag but can be employed for separation control. Direct numerical simulations (DNS) and large-eddy simulations (LES) of uniform blowing and suction applied to turbulent boundary layers have also been performed (Park and Choi, 1999; Kim et al., 2002; Kametani and Fukagata, 2011; Kametani et al., 2015; Bobke et al., 2016). In most cases, these simulations were carried out in zero-pressure-gradient conditions to investigate the effects of blowing and suction on dynamics of wall-bounded turbulence. For instance, Stroh et al. (2016) compared uniform blowing and suction with body-force damping (as a model of opposition control) and introduced the concept of virtual origin to describe blowing and suction effects in the downstream of the control region.

*Corresponding author: liweipeng@sjtu.edu.cn

Recently, researchers have taken interests in the blowing and suction control of TBLs on wing sections. Using mass suction at the leading edge of a Clark-Z airfoil to provide pressurized air for blowing, Kornilov (2017) studied uniform blowing on the pressure side of the airfoil at Reynolds number $Re_c=U_\infty c/\nu=840,000$, where U_∞ is the incoming flow velocity, c is the chord length, and ν is the fluid kinematic viscosity. Eto et al. (2019) studied the effects of both active and passive blowing on the suction side of a Clark-Y airfoil at $Re_c=1,500,000$. Kornilov et al. (2019) employed blowing on the pressure side and suction on the suction side of a NACA0012 airfoil, and later they provided an estimation of the control energy cost under the same conditions (Kornilov, 2021). Mahfoze et al. (2019) used Bayesian optimization to discuss how to benefit from downstream effects of blowing when the control region is separated into individual areas. The first high-fidelity numerical simulation of a wing section with uniform blowing was reported by Vinuesa and Schlatter (2017), although at a low Reynolds number ($Re_c=100,000$). Soon after, Atzori et al. (2020) presented a dataset of highly-resolved LES of a NACA4412 airfoil at $Re_c=200,000$ and $400,000$ with various configurations of uniform blowing and suction, using as a reference the simulation carried out by Vinuesa et al. (2018). This dataset has been later employed by Fahland et al. (2021) to validate Reynolds-Averaged Navier–Stokes (RANS) simulations, and it is also considered in the present paper.

The key objective of this study is to investigate the control effects on mean friction drag on a wing section with uniform blowing and suction. Although the mean friction drag is a wall property, as can be directly calculated from the normal gradient of the mean tangential velocity at the wall, it is connected to the statistical turbulence quantities across the wall layer and can be further decomposed into various physics-informed components according to different mathematical derivations and physical interpretations (Li et al., 2019; Fan et al., 2019a,b). So far, there have been three kinds of friction-drag decomposition methods, derived from the momentum, vorticity, and energy balance, respectively. The first one is the so-called Fukagata-Iwamoto-Kasagi (FIK) identity (Fukagata et al., 2002), in which a triple integration is performed on the mean momentum balance equation and gives a direct relationship between the skin-friction coefficient and the Reynolds-shear-stress profile. The FIK identity has been widely used and extended for more complex situations over the years, e.g. Mehdi and White (2011); Mehdi et al. (2014); Modesti et al. (2018); Peet and Sagaut (2009); Bannier et al. (2015), to name a few. Kametani et al. (2015) and Stroh et al. (2015) applied FIK identity to quantify the variation of skin-friction coefficients caused by blowing and suction in ZPG-TBLs. Inspired by the mathematical derivation of FIK identity, Yoon et al. (2016) derived a vorticity-based formula relating the mean friction-drag generation with the motion of vortical structures, by performing a triple integration on the mean spanwise vorticity transport equation. They later used this method to analyze the contribution of outer large-scale motions to the friction-drag generation in a moderate APG-TBL (Yoon et al., 2018). Finally, an energy-based decomposition method was proposed by Renard and Deck (2016) from the perspective of streamwise kinetic energy balance. Under an absolute reference frame where the wall is moving, the friction drag develops a non-zero power, which is characterized as the energy transferred from the wall to the fluid, by means of molecular viscosity dissipation, turbulence-kinetic-energy production, and spatial growth of the flow. This method is referred to as RD identity hereafter. The RD identity has been used to analyze the friction-drag generation in channel flows, ZPG/APG-TBLs, turbulent square-duct flows, and pipe flows (Fan et al., 2019a,b, 2020a,b; Wei, 2018). Li et al. (2019) and Fan et al. (2019b) generalized the RD identity to a compressible form to quantify the compressibility effects on the friction-drag generation. All these three methods (Fukagata et al., 2002; Yoon et al., 2016; Renard and Deck, 2016) are mathematically correct and have been widely validated. In the present study, we only adopt the RD identity, considering that the momentum- and vorticity-based method (by three successive integrations) are lack of physics-informed interpretations, thus their decomposed constituents hardly carry the causal relationship for the friction-drag generation (Deck et al., 2014; Renard and Deck, 2016; Fan et al., 2019a).

The turbulent boundary layers on the suction/pressure sides of the wing section are subjected to adverse/favorable pressure gradients. The pressure gradients have significant impacts on the scales of coherent structures across

the wall layer. For instance, inner-outer scale separation is more evident in APG-TBLs than in ZPG-TBLs, even at relatively low Reynolds numbers, due to the enhancement of outer-scale motions (Tanarro et al., 2020). Additionally, a significant increment of small-scale energy was found in the outer region, as the vertical motion induced by the APG transports small scales from the near-wall region to the outer layer (Vinueza et al., 2018; Tanarro et al., 2020). In the present study, we also aim to quantify the contribution of structures with different scales to the generation of friction drag on the wing section with/without blowing and suction. Studies on such cases are likely to promote new drag control strategies. To this end, an appropriate approach to separate the multi-scale coherent structures is in need. Typically, Fourier analysis might be a tempting tool to decompose the raw signals into modes with given wavelengths, yet it relies on *a-priori* definition of cutoff wavelength and suffers from inflexibility for complex and transient signals (Cheng et al., 2019). Another frequently-used method is proper orthogonal decomposition (POD) (Lumley, 1967; Wu and Christensen, 2010), which sorts the contribution of velocity fluctuations to the turbulence kinetic energy. However, Wang et al. (2018, 2019) pointed out that, the energy-ranking spatial modes cannot fully recover the dynamics of turbulent motions in different length scales. In contrast, empirical mode decomposition (EMD), proposed by Huang et al. (1998), provides an adaptive, data-driven, and *a-posteriori* technique to delineate the transient and local characteristics of signals. It is in principle free from pre-established basis functions and represents the original signal as a superposition of several mono-components and a residual, with the characteristic wavelengths of the signals automatically determined. With EMD, Huang et al. (2008) studied the scaling properties and intermittency of homogeneous turbulence, and Ansell and Balajewicz (2017) analyzed the features of large-scale vortical structures in a turbulent mixing layer. Agostini and Leschziner (2014, 2016) used bidimensional empirical mode decomposition (BEMD) to analyze the modulation of large-scale motions on the small-scale eddies in the near-wall region, and later they discussed the scale-specific contributions of large- and small-scale structures to the friction-drag generation by means of FIK and RD identity (Agostini and Leschziner, 2019) in channel flows. Dogan et al. (2019) have used EMD to characterize the inner-outer interaction based on the modulation coefficient. Cheng et al. (2019) adopted BEMD to identify attached eddies in turbulent channel flows and quantify their relationship with the friction-drag generation. However, no relevant study has been found in the open literature to analyze the scale-specific contribution of turbulent motions to friction-drag generation on the wing section with/without blowing and suction.

This paper is organized as follows. In Sec.2, we introduce the friction-drag decomposition method and the database of flow over a NACA4412 airfoil. The decomposition results on the suction and pressure side of the NACA4412 are discussed in Sec. 3 and 4, respectively. Concluding remarks are given in Sec. 5.

2 Friction-drag decomposition method and the database of flow over the NACA4412 airfoil

With the energy-based RD identity (Renard and Deck, 2016), the skin-friction coefficient C_f of a turbulent boundary layer can be decomposed as:

$$C_f = \underbrace{\frac{2}{U_e^3} \int_0^\infty v \left(\frac{\partial \langle u \rangle}{\partial y} \right)^2 dy}_{C_{f,v}} + \underbrace{\frac{2}{U_e^3} \int_0^\infty -\langle u'v' \rangle \frac{\partial \langle u \rangle}{\partial y} dy}_{C_{f,t}} + \underbrace{\frac{2}{U_e^3} \int_0^\infty (\langle u \rangle - U_e) \frac{\partial}{\partial y} \left(v \frac{\partial \langle u \rangle}{\partial y} - \langle u'v' \rangle \right) dy}_{C_{f,G}}, \quad (1)$$

where $\langle \cdot \rangle$ is the Reynolds averaging operator, the prime ' denotes fluctuations with respect to the Reynolds averages, U_e is the velocity at the boundary-layer edge δ_{99} , x and y represent the directions tangential and

normal to the wall surface respectively, and u and v are the corresponding velocity components. The derivation of the RD identity can be retrieved in [Renard and Deck \(2016\)](#).

Three contributive friction constituents are obtained in equation (1). Thereinto, (i) $C_{f,V}$ represents the direct molecular viscous dissipation, transforming the mechanical power into heat; (ii) $C_{f,T}$ represents the power spent for turbulence-kinetic-energy production; (iii) $C_{f,G}$ accounts for the spatial growth of the flow, which is also interpreted as the rate of gain of mean streamwise kinetic energy by the fluid in the absolute frame. Note that the integrand in $C_{f,G}$ has been substituted with local information which only depends on the well-documented wall-normal profiles ([Renard and Deck, 2016](#)). This is especially applicable for the cases where the accurate calculation of explicit streamwise derivatives is unfeasible.

For adverse-/favorable-pressure-gradient turbulent boundary layers around an airfoil, the roles of the wall-normal convection and pressure gradient are of particular importance and should be individually discussed, thus a further decomposition of $C_{f,G}$ is carried out, *viz.*

$$C_{f,G} = \underbrace{\frac{2}{U_e^3} \int_0^\infty (\langle u \rangle - U_e) \left(\langle v \rangle \frac{\partial \langle u \rangle}{\partial y} \right) dy}_{C_{f,C}} + \underbrace{\frac{2}{U_e^3} \int_0^\infty (\langle u \rangle - U_e) I_x dy}_{C_{f,D}} + \underbrace{\frac{2}{U_e^3} \int_0^\infty (\langle u \rangle - U_e) \left(\frac{dp/\rho}{dx} \right) dy}_{C_{f,P}}, \quad (2)$$

where $I_x = \partial \langle u' u' \rangle / \partial x + \langle u \rangle \partial \langle u \rangle / \partial x - \nu \partial^2 \langle u \rangle / \partial x^2$, p is the static pressure, and ρ is the density. Contributions of the mean wall-normal convection ($C_{f,C}$), streamwise development ($C_{f,D}$), and the pressure gradient ($C_{f,P}$) are separated in equation (2).

We consider a set of well-resolved LESs of a NACA4412 airfoil at angle of attack of 5° at two chord Reynolds numbers, *i.e.* $Re_c=200,000$ and $400,000$. The simulations were performed with the spectral-element code *Nek5000*, developed by [Fischer et al. \(2008\)](#). The spatial derivatives in the incompressible Navier–Stokes equations are discretized employing a Galerkin method, following the $P_N - P_{N-2}$ formulation by [Patera \(1984\)](#) and the solution is expressed within each spectral element in terms of a nodal-base of Legendre polynomials on the Gauss–Lobatto–Legendre (GLL) quadrature points. The discretization of the time derivatives is explicit for the non-linear terms and implicit for the viscous term, employing an extrapolation and a backward differentiation scheme, respectively, both of the third order. In order to trigger transition to turbulence, we employed tripping through a volume force, implemented as proposed by [Schlatter and Örlü \(2012\)](#), at $x/c = 0.1$ on both suction and pressure sides.

The cases with/without control, listed in Table 1, include various configurations of uniform blowing and suction applied on the suction side and uniform blowing applied on the pressure side. The relative proportions of pressure drag and skin-friction drag determine the control effects on the total drag, denoted by c_d . At these moderate Reynolds numbers, pressure drag is relatively high and uniform blowing on the suction side increases it by an amount that is high enough to overcome the skin-friction reduction, eventually leading to higher c_d . On the contrary, uniform suction increases skin-friction drag, but it decreases the pressure drag enough to result in lower c_d . At the same time, uniform blowing and suction on the suction side also decreases and increases lift (c_l), respectively. Uniform blowing on the pressure side has different effects on the pressure distribution around the airfoil, decreasing both skin friction and pressure drag and increasing lift. The friction Reynolds numbers ($Re_\tau = u_\tau \delta_{99} / \nu$) and the Rotta-Clauser pressure-gradient parameters ([Rotta, 1950](#); [Clauser, 1954, 1956](#)) ($\beta = \delta^* / \tau_w dPe/dx$) are also listed in Table 1. Note that $u_\tau = \sqrt{(\tau_w / \rho)}$ is the friction velocity, δ^* is the displacement thickness, τ_w is the wall shear stress, and dPe/dx is the streamwise pressure gradient at the boundary-layer edge. For a more complete description of the numerical setup and the aerodynamic effects of control, we refer to [Vinuesa et al. \(2018\)](#) and [Atzori et al. \(2020\)](#).

Case	Control strategies	Intensity (V_{wall})	$\Delta(c_l)$	$\Delta(c_d)$	$\Delta(L/D)$	Re_τ	β
<i>Re200k, ss, ref</i>	–	–	–	–	–	[132, 224]	[0.16, 11.07]
<i>Re200k, ss, blw1</i>	blowing, suction s. ($0.25 < x/c < 0.86$)	$0.1\%U_\infty$	–4%	+3%	–7%	[126, 209]	[0.14, 19.62]
<i>Re200k, ss, blw2</i>	blowing, suction s. ($0.25 < x/c < 0.86$)	$0.2\%U_\infty$	–8%	+8%	–15%	[118, 193]	[0.12, 36.54]
<i>Re200k, ss, sct1</i>	suction, suction s. ($0.25 < x/c < 0.86$)	$0.1\%U_\infty$	+4%	–2%	+6%	[139, 238]	[0.17, 6.97]
<i>Re200k, ss, sct2</i>	suction, suction s. ($0.25 < x/c < 0.86$)	$0.2\%U_\infty$	+7%	–4%	+11%	[145, 248]	[0.18, 4.71]
<i>Re400k, ss, ref</i>	–	–	–	–	–	[183, 363]	[0.15, 9.16]
<i>Re400k, ss, blw1</i>	blowing, suction s. ($0.25 < x/c < 0.86$)	$0.1\%U_\infty$	–4%	+5%	–9%	[174, 335]	[0.14, 17.56]
<i>Re400k, ss, sct1</i>	suction, suction s. ($0.25 < x/c < 0.86$)	$0.1\%U_\infty$	+3%	–1%	+4%	[193, 390]	[0.15, 5.37]
<i>Re200k, ps, ref</i>	–	–	–	–	–	[96, 219]	[–0.30, –0.01]
<i>Re200k, ps, blw1</i>	blowing, pressure s. ($0.2 < x/c < 1.00$)	$0.1\%U_\infty$	+0%	–3%	+4%	[87, 232]	[–0.42, –0.03]
<i>Re200k, ps, blw2</i>	blowing, pressure s. ($0.2 < x/c < 1.00$)	$0.2\%U_\infty$	+1%	–5%	+7%	[80, 234]	[–0.55, –0.04]

Table 1: Cases with/without control considered in the present paper and the relative changes of the total lift and drag coefficients (denoted by $\Delta(c_l)$ and $\Delta(c_d)$, respectively) and aerodynamic efficiency (denoted by $\Delta(L/D)$) in respect to the reference case. Note that “suction s.” and “pressure s.” are suction and pressure sides, respectively, *Re200k* and *Re400k* are the chord Reynolds number (Re_c) of each case, Re_τ denotes the friction Reynolds number, and β is the Rotta-Clauser pressure-gradient parameter.

3 Friction-drag decomposition on the suction side

3.1 The control effects

Using the database, we first show the variation of skin-friction coefficients on the suction side of a NACA4412 wing section in figure 1. It can be easily found that uniform blowing causes friction-drag reduction whereas suction causes friction-drag increase, regardless of the Reynolds number and streamwise position on the control surface. Stronger intensity of blowing/suction leads to larger drag-reduction/increase rate, as expected. Such phenomena are in consistence with previous studies (Kametani and Fukagata, 2011; Kametani et al., 2015; Atzori et al., 2020). The mechanisms of the drag reduction/increase by blowing/suction are associated with the interactions between the “cross-stream” and the quasi-streamwise vortical structures in the near-wall region, which probably enhance or damp the behavior of sweep/ejection events and yield modifications of the mean velocity profiles (Park and Choi, 1999; Kim et al., 2002; Hwang, 2004; Kornilov, 2015). The variation of turbulent dynamics in the near-wall region leads to a redistribution of the turbulence kinetic energy and alteration of the turbulent momentum transport across the wall layer. The vortical structures in the outer layer will also be influenced by the near-wall blowing/suction, especially in the downstream of the control surface. Consequently, the generation of the skin-friction drag, which is linked to the turbulence statistics across the wall layer, will be correspondingly changed.

In order to clarify such control effects, we conduct the decomposition of skin-friction coefficients on the suction side (within $0.2 \leq x/c \leq 0.85$) of NACA4412 by RD identity. Note that the relative errors, $(C_{f,V} + C_{f,T} + C_{f,G} - C_f)/C_f$, where C_f is directly calculated with the normal gradient of tangential velocity at the wall surface (i.e. $C_f = (\mu \partial \langle u \rangle / \partial y)|_{wall} / (0.5 \rho U_e^2)$), are well confined within $\pm 0.12\%$ for all cases considered, which confirms the reliability of the decomposition method.

Figure 2 shows the variations of $C_{f,V}$, $C_{f,T}$, and $C_{f,G}$ induced by uniform blowing and suction with regard to the reference case, at $Re_c=200,000$ (figures 2(a)–2(c)) and $Re_c=400,000$ (figures 2(d)–2(f)). With blowing, the friction contribution of direct viscous dissipation ($C_{f,V}$) is reduced at both Reynolds numbers. This is closely related to the suppression of the near-wall sweep events, which transport high-speed fluid towards the wall. With blowing, an increase of the generation of turbulence-kinetic-energy production ($C_{f,T}$) is found in figures 2(b) and 2(e). The variations of $C_{f,V}$ and $C_{f,T}$ are essentially associated with the influences on the wall-normal profiles of mean viscous shear stress and Reynolds shear stress across the wall layer, which will be discussed

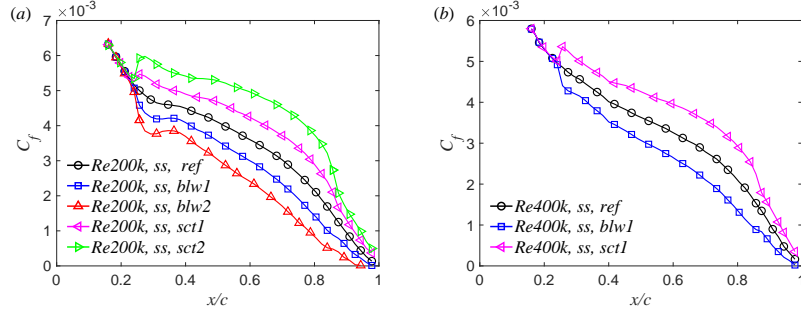


Figure 1: Variation of skin-friction coefficients on the suction side of a NACA4412 wing section at (a) $Re_c = 200,000$ and (b) $Re_c = 400,000$.

in Sec. 3.2.

As for the generation of the spatial growth ($C_{f,G}$), it is decreased by the blowing and the influence on $C_{f,G}$ is stronger than that on $C_{f,V}$ and $C_{f,T}$. To further clarify the cause of such variation, we trace back to its sub-constituents in equation (2) and plot the variations of $C_{f,C}$, $C_{f,D}$, and $C_{f,P}$ in figure 3. In the cases with blowing, the generation of wall-normal convection ($C_{f,C}$) and adverse pressure gradient ($C_{f,P}$) is decreased, while that of streamwise development ($C_{f,D}$) is increased. A slight turnup of $C_{f,P}$ is observed near the trailing edge for the blowing cases (see figure 3(c)), which probably relates to the fact that the boundary layer is approaching the condition of mean separation (Atzori et al., 2020). Generally, the positive variation of $C_{f,D}$ is overcome by the negative influence on $C_{f,C}$ and $C_{f,P}$, which consequently leads to the overall reduction of $C_{f,G}$ by blowing (Mahfoze et al., 2019), as shown in figures 2(c) and 2(f). In Sec. 3.2, we will further analyze the wall-normal distributions of these friction constituents, to reveal the connection of the C_f -constituents with the turbulent dynamics across the boundary layer. With mass suction, the control effects on the C_f -constituents shown in figure 2 and 3 are opposite to those with blowing. Here we did not add more discussions on the suction cases for brevity.

In order to assess the control effects on the total skin-friction drag over the control surface, a parameter $\bar{D}_{f,i}$ is introduced:

$$\bar{D}_{f,i} = \int_{\Omega_{\text{ctr}}} \tau_{w,i} (\vec{t} \cdot \vec{n}) d\xi, \quad (3)$$

where $\tau_{w,i} = C_{f,i} \cdot (0.5\rho U_e^2)$ is the decomposed component of wall-shear stress, with the subscript ‘ i ’ working as a label to denote each C_f -constituent, *i.e.* ‘ V ’, ‘ T ’, ‘ G ’, ‘ C ’, ‘ D ’, and ‘ P ’ as mentioned in equations (1) and (2), \vec{t} and \vec{n} denote the unit vectors tangential to the airfoil surface and along the free-stream direction respectively, ξ is the curvilinear coordinate along the airfoil surface, and Ω_{ctr} represents the area of the control surface. The change rate of $\bar{D}_{f,i}$, with respect to the uncontrolled reference case, is then defined as:

$$R_i = \frac{(\bar{D}_{f,i} - \bar{D}_{f,i}^{\text{ref}})}{\bar{D}_f^{\text{ref}}}. \quad (4)$$

Figure 4 shows the result of R_i under different control schemes at $Re_c=200,000$ and $400,000$. It can be seen that R_i appears to be linearly dependent on the control intensity of the blowing/suction, within $-0.2\% \leq V_{\text{wall}}/U_\infty \leq 0.2\%$. However, note that this might not always be true when V_{wall}/U_∞ becomes much larger, and needs to be validated in the future work. Among the decomposed constituents, the most significant control effect lies on the friction constituent of spatial growth of the flow ($C_{f,G}$), with its sub-constituents primarily correlated with the convection, streamwise growth, and pressure gradient in the outer region (Fan et al., 2020a). This reveals that the tremendously influenced outer-layer dynamics play an important role in the drag control

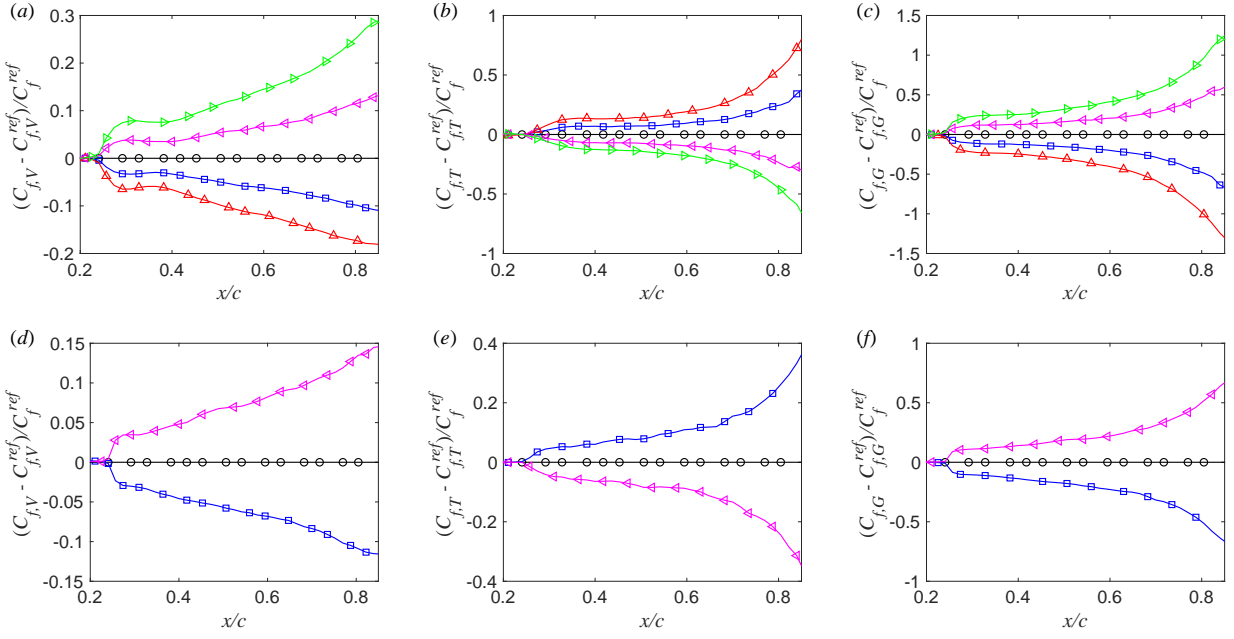


Figure 2: Variation of (a, d) $C_{f,V}$, (b, e) $C_{f,T}$, and (c, f) $C_{f,G}$ with regard to the reference case on the suction side of a NACA4412 wing section at (a – c) $Re_c = 200,000$ and (d – f) $Re_c = 400,000$. (The superscript of “ref” represents the reference case without control. Legends in (a – c) refer to figure 1(a), while those in (d – f) refer to figure 1(b).)

with blowing/suction. Moreover, weak Reynolds-number effects are found, especially for R_V and R_G , where a stronger control effect is achieved at higher Reynolds number which to some extent validates the theoretical estimation by Kametani and Fukagata (2011).

3.2 Wall-normal distributions of the C_f -constituents

To answer the question that how uniform blowing/suction specifically influences the sources of skin-friction generation, the wall-normal distributions of the decomposed C_f -constituents across the boundary layer are investigated. As C_f and its constituents vary along the streamwise direction on the wing surface, we only discuss the wall-normal contributions of the C_f -constituents at $x/c \approx 0.75$, where the friction Reynolds numbers are $Re_\tau \approx 224, 205, 180, 237, 245, 362, 332,$ and 387 in the case of “Re200k, ss, ref”, “Re200k, ss, blw1”, “Re200k, ss, blw2”, “Re200k, ss, sct1”, “Re200k, ss, sct2”, “Re400k, ss, ref”, “Re400k, ss, blw1”, and “Re400k, ss, sct1” respectively. Similar conclusions can be drawn at other positions within $0.2 \leq x/c \leq 0.85$, and the results are not shown here for simplicity.

The C_f -constituents are expressed in intrinsic scales as:

$$C_{f,V} = 2/U_e^+ \int_0^\infty \left(\frac{\partial \langle u \rangle^+}{\partial y^+} \right)^2 dy^+, \quad (5)$$

$$C_{f,T} = 2/U_e^+ \int_0^\infty \langle -u'v' \rangle^+ \frac{\partial \langle u \rangle^+}{\partial y^+} dy^+, \quad (6)$$

$$C_{f,G} = 2/U_e^+ \int_0^\infty (\langle u \rangle^+ - U_e^+) \frac{\partial}{\partial y^+} \left(\frac{\partial \langle u \rangle^+}{\partial y^+} - \langle u'v' \rangle^+ \right) dy^+, \quad (7)$$

where the superscript + denotes normalization by viscous units, *i.e.* friction velocity u_τ and viscous length scale

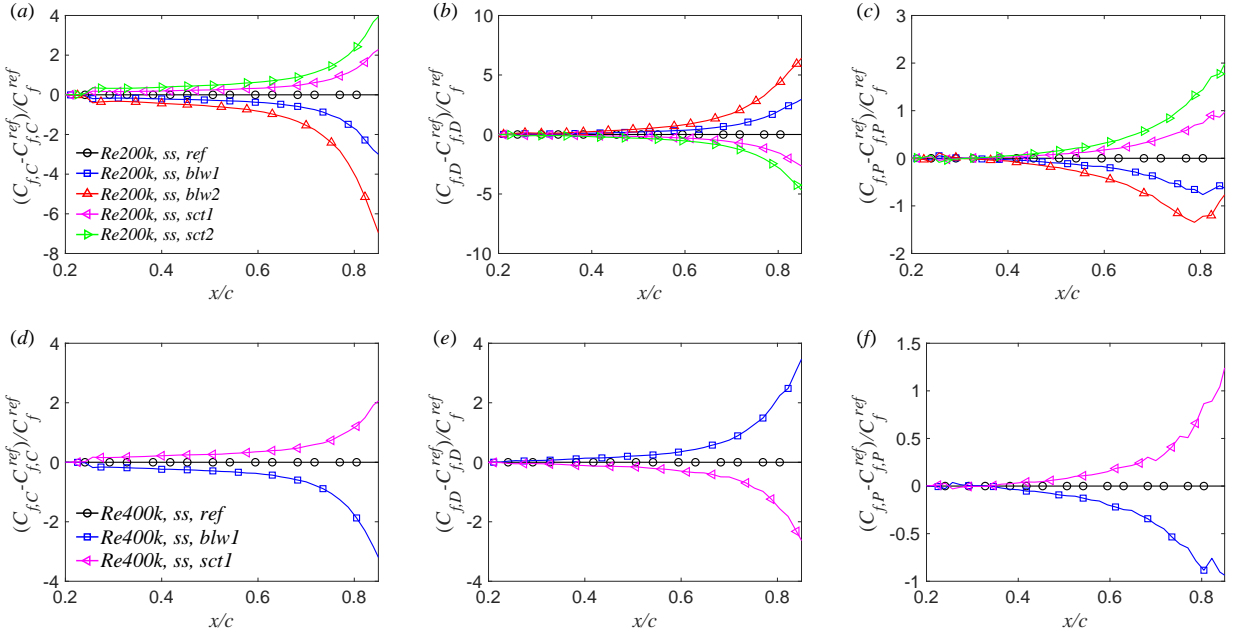


Figure 3: Variation of (a, d) $C_{f,C}$, (b, e) $C_{f,D}$, and (c, f) $C_{f,P}$ with regard to the reference case on the suction side of a NACA4412 wing section at (a – c) $Re_c = 200,000$ and (d – f) $Re_c = 400,000$.

$$\delta_v = \nu/u_\tau.$$

Figure 5 shows the wall-normal distributions of the pre-multiplied integrand of $C_{f,V}$, $C_{f,T}$, and $C_{f,G}$ in equations (5)–(7), as a function of y^+ . The semi-logarithmic plots retain the advantage that the areas beneath the curves directly yield the total generation of the constituents. Comparisons between figures 5(a)–5(c) for the cases at $Re_c=200,000$ and 5(d)–5(f) for the cases at $Re_c=400,000$ confirms that the Reynolds-number variation does not change the conclusions which will be presented in the following from a qualitative perspective.

For the distribution of $C_{f,V}$ -contributions, two peaks are respectively observed in the near-wall and outer region of APG-TBLs. Most of the $C_{f,V}$ -contributions come from the inner region ($y^+ < 30$), indicating that the viscous dissipation is mostly concentrated in the near-wall region, as expected. In the meantime, a secondary peak appears in the outer region, which is probably due to the energy enhancement by APG (Tanarro et al., 2020; Sanmiguel Vila et al., 2020). The secondary peak is absent in the ZPG-TBLs even at higher friction Reynolds number up to $Re_\tau = 1270$ (Fan et al., 2019b). When uniform blowing/suction is applied, the locations of inner peaks are fixed at a wall-normal distance of $y^+ \approx 5.0 - 6.0$, regardless of the control scheme. In the blowing cases, the inner peak of $C_{f,V}$ -contributions is reduced whereas the outer peak is increased, suggesting a lowered mean shear in the near-wall region while enhanced in the outer region due to the lifting-up of boundary layer (Kornilov, 2015), which is also validated by showing the wall-normal gradient of the tangential velocity in figures 6(a) and 6(c). This reveals that blowing has different actions in different sub-layers, namely inhibiting the contribution of inner-layer dynamics to skin-friction generation while promoting that of outer-layer dynamics. When blowing intensity is up to 0.2%, the outer-layer contributions seem to be comparable to the inner-layer contributions. On the other hand, suction behaves quite opposite for all constituents, which will not be repeated hereafter.

Similar inner and outer peaks are also observed in the pre-multiplied distribution of $C_{f,T}$ -contributions, as shown in figures 5(b) and 5(e), with the former well collapsed at the inner-scaled wall-normal distance $y^+ \approx 16.0 - 17.0$. It can be found that the outer-layer motions dominate the contributions of $C_{f,T}$, although the Re_τ is lower than 400, which is much different from the features in ZPG-TBLs (Fan et al., 2019b). The

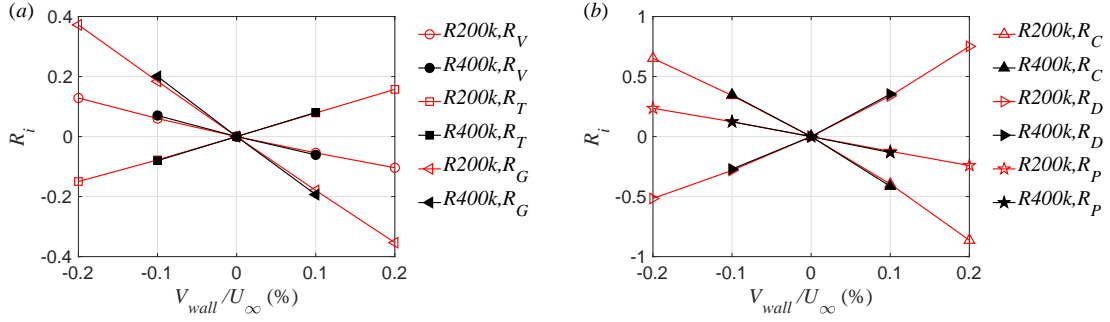


Figure 4: Total friction-drag change rate as a function of control intensity (V_{wall}/U_∞) on the suction side of a NACA4412 wing section.

prominent peak in the outer region suggests the energization of large-scale outer motions by APGs (Harun et al., 2013). When blowing is applied, the inner peak of $C_{f,T}$ -contributions is reduced, while the outer peak is increased. This phenomenon is linked to the wall-normal distributions of the wall-normal velocity gradient and Reynolds shear stress, as shown in figure 6. With blowing, the wall-normal velocity gradients are suppressed significantly in the near-wall region, probably resulting from the damping of the near-wall sweep motions. On the other hand, in the outer layer, the Reynolds shear stress is amplified by the blowing. These two actions are consequently responsible for the changes of the inner and outer peaks in the distribution of $C_{f,T}$ -contributions.

As for the distribution of $C_{f,G}$ -contributions in figures 5(c) and 5(f), negative contributions are observed within $y^+ \lesssim 80$ for the uncontrolled reference case at $Re_c=200,000$ ($y^+ \lesssim 130$ at $Re_c=400,000$), and positive values beyond this region. This differs from the result in ZPG-TBLs: $C_{f,G}$ always remains positive across the wall layer (Fan et al., 2020a). Blowing enhances both the negative and positive distributions, as the strengthened adverse pressure gradient promotes a more pronounced growth of the boundary layer and a more prominent outer region (Vinuesa et al., 2018).

In contrast to the wall-normal distributions as a function of y^+ shown in figure 5, figure 7 plots their profiles as a function of y/δ_{99} . The outer-peak locations of $C_{f,V-}$, $C_{f,T-}$, and $C_{f,G}$ -contributions normalized by the outer scale are well-collapsed at $y/\delta_{99} \approx 0.7$, 0.53 , and 0.65 , respectively, as marked with vertical dashed lines in figure 7, regardless of the control scheme and Reynolds number. These phenomena are consistent with our previous finding (Fan et al., 2020a), *i.e.* the inner-peak locations (in $C_{f,V-}$ and $C_{f,T-}$ -contribution) exhibit good scaling in the inner unit (δ_y), and the outer-peak locations in the outer unit (δ_{99}), regardless of the friction Reynolds number, the magnitude of APG and its development history. This finding suggests that self similarity is exhibited in inner or outer scales for the turbulence statistics associated with the friction-drag generation.

The generation of $C_{f,G}$ results from a counterbalance between the negative work done by $C_{f,C}$ and $C_{f,P}$ and the positive work by $C_{f,D}$. Figure 8 quantifies their wall-normal distributions, and only the outer scaling by δ_{99} is applied herein. Good collapses of the peak locations are also observed at $y/\delta_{99} \approx 0.59$, 0.56 , and 0.43 for $C_{f,C-}$, $C_{f,D-}$, and $C_{f,P-}$ contributions, respectively. In the blowing cases, the APG effects, a fact that promotes the population/energization of outer-layer structures (Harun et al., 2013), are strengthened. Meanwhile, the wall-normal convection and the streamwise boundary-layer growth are intensified in the outer region (Vinuesa et al., 2018). Therefore, in an absolute sense, the generations of the components ($C_{f,C}$, $C_{f,D}$, and $C_{f,P}$) are all enhanced. Thereinto, as the convection and pressure gradient do negative work for the friction-drag generation, blowing acts to reduce the $C_{f,C-}$ and $C_{f,P-}$ contributions. On the other hand, the positive contribution of $C_{f,D}$ is increased, as shown in figures 8(b) and 8(e). These three components counterbalance each other. The negative $C_{f,C-}$ and $C_{f,P-}$ contributions are responsible for the $C_{f,G}$ reduction in the near-wall region, whereas the positive $C_{f,D-}$ contributions is responsible for the increase of $C_{f,G}$ in the outer region, as seen in figures 5(c) and 5(f).

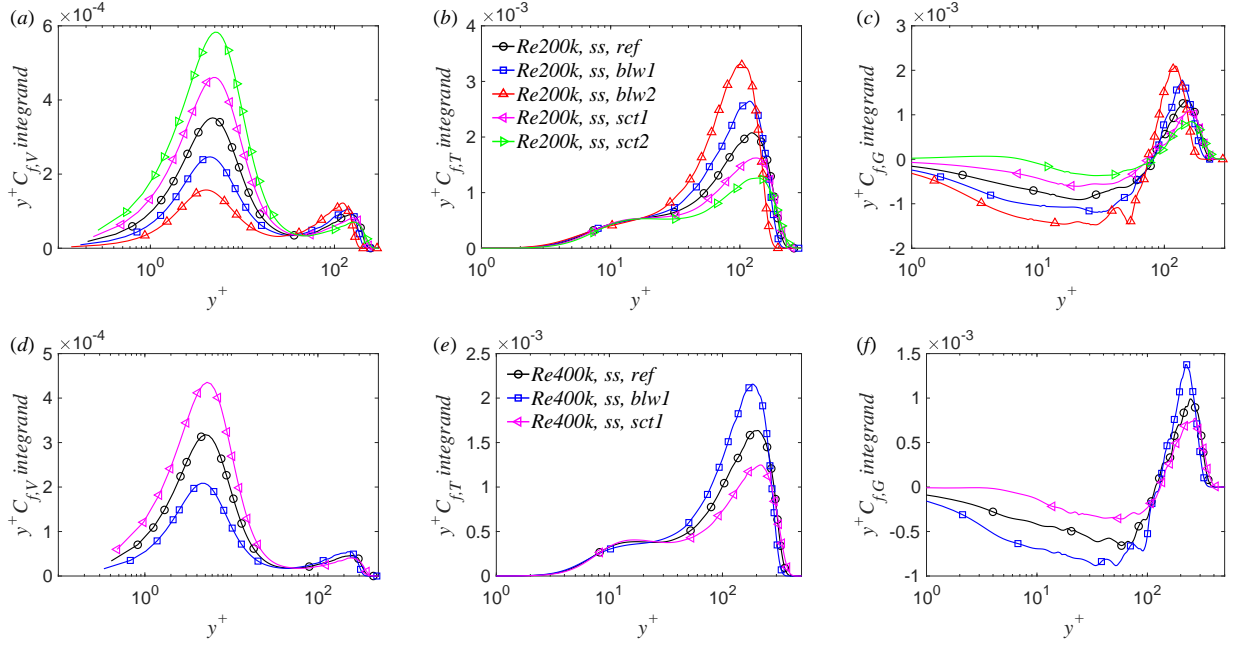


Figure 5: Pre-multiplied integrands of (a, d) $C_{f,V}$, (b, e) $C_{f,T}$, and (c, f) $C_{f,G}$ at $x/c \approx 0.75$, as a function of y^+ , on the suction side of a NACA4412 wing section at (a – c) $Re_c = 200,000$ and (d – f) $Re_c = 400,000$.

3.3 Contributions of small- and large-scale structures to the friction-drag generation

Firstly, we use empirical mode decomposition (EMD) (Huang et al., 1998) to identify the small- and large-scale turbulence structures. EMD is an adaptive mode-decomposition technique, which extracts characteristic wavelengths of non-stationary signals automatically without *a-priori* basis functions. It has been applied for wall-bounded turbulence (Agostini and Leschziner, 2014, 2019; Cheng et al., 2019; Dogan et al., 2019), and details of the methodology of EMD can be found in Huang et al. (1998). Here we just describe EMD very briefly.

With EMD, a raw temporal or spatial signal $f(t)$ is decomposed into a sum of multiple intrinsic mode functions (IMFs) with a residual $R(t)$:

$$f(t) = \sum_{i=1}^m \text{IMF}_i(t) + R(t), \quad (8)$$

where m is the number of IMFs. The IMFs are data-driven functions, representing components with different wavelengths or scales in the full field. In this study, the velocity fluctuations (u' and v') at the streamwise location $x/a \approx 0.75$ are decomposed into four modes (three IMFs with a final residual). The first two modes represent the small-scale structures and the others characterize the large scales, which is justified based on a preliminary analysis (similar to the studies of Agostini and Leschziner (2014, 2019)).

The contours of spanwise pre-multiplied spectra of u' and v' scaled with friction velocities are plotted in figure 9 for the $Re_c=400,000$ cases. Similar features can also be found in the low-Reynolds-number ($Re_c=200,000$) cases, which are not shown here for brevity. In figure 9, the iso-contour levels marked with dashed and solid lines represent the spectra of small- and large-scale velocity fluctuations, respectively. These contour lines indicate 0.12, 0.42, and 0.72 of their maxima, from outside to inside. For the reference case, as shown in figure 9(a), the spectra of small-scale u' -structures peak at the wall-normal distance $y^+ \approx 10$ with a spanwise wavelength $\lambda_z^+ \approx 80$, and those of large-scale u' -structures peak at $y^+ \approx 100$ ($y/\delta_{99} \approx 0.28$) with

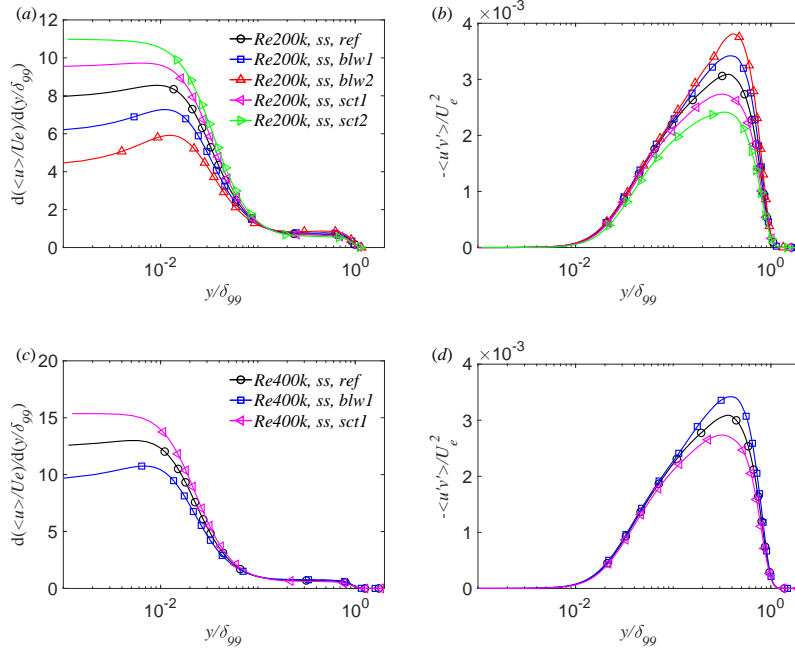


Figure 6: Profiles of (a, c) wall-normal velocity gradient and (b, d) Reynolds shear stress, on the suction side of a NACA4412 wing section at (a, b) $Re_c = 200,000$ and (c, d) $Re_c = 400,000$.

$\lambda_z^+ \approx 310$ ($\lambda_z/\delta_{99} \approx 0.85$). This observation is consistent with the study of Cheng et al. (2019), that small-scale u' -structures identified by EMD are representative of the near-wall coherent motions, whereas the large-scale u' -structures characterize large-scale motions.

When blowing/suction is applied on the airfoil surface, such energy spectra are affected, as seen in figures 9(b) and 9(c). In the case of blowing, the small-scale structures are enhanced, and penetrate deeper into the outer region. The peak of spectra locates at $(\lambda_z^+, y^+) \approx (80, 8)$. Whereas suction has the opposite influence on the amplitude of small scales, with the peak location faintly influenced at $(\lambda_z^+, y^+) \approx (90, 10)$. As for the large-scale structures, they are enhanced by blowing, due to the energized large-scale motions, which agrees well with the conclusion drawn by Kametani et al. (2015). The peak of large-scale spectra locates at $(\lambda_z/\delta_{99}, y/\delta_{99}) \approx (0.96, 0.33)$. As shown in figure 9(c), suction trends to diminish the secondary peak in the outer region with the peak at $(\lambda_z/\delta_{99}, y/\delta_{99}) \approx (0.93, 0.35)$.

As for the v' -structures shown in figures 9(d)–9(f), the small- and large-scale structures have approximately the same spanwise wavelengths as the u' -structures, which is consistent with the EMD results of channel flows (Cheng et al., 2019), suggesting that the decomposed two scales of u' - and v' -structures can be characterized with the same spanwise wavelength. Both the small- and large-scale v' -structures are greatly enhanced by blowing while reduced by suction. On the other hand, the wall-normal locations of the v' -structures are much different from those of u' -structures, because that the presence of wall prevents the normal velocity fluctuations from extending close to the near-wall region, in contrast to the wall-parallel component u' . As shown in figures 9(d)–9(f), the small-scale spectra of v' are more intense beyond the buffer layer at $y^+ \approx 50$, with the spanwise wavelength scale λ_z^+ peaking at around 80–100 for all of the three cases, and the large-scale v' -spectra peak around $(\lambda_z/\delta_{99}, y/\delta_{99}) \approx (0.9, 0.35)$.

Hereafter, we denote the small- and large-scale tangential and wall-normal velocity fluctuations as $u'_s, u'_l, v'_s,$ and v'_l , respectively. Then the Reynolds stress is decomposed as:

$$-\langle u'v' \rangle = -\langle u'_s v'_s \rangle - \langle u'_s v'_l \rangle - \langle u'_l v'_s \rangle - \langle u'_l v'_l \rangle, \quad (9)$$

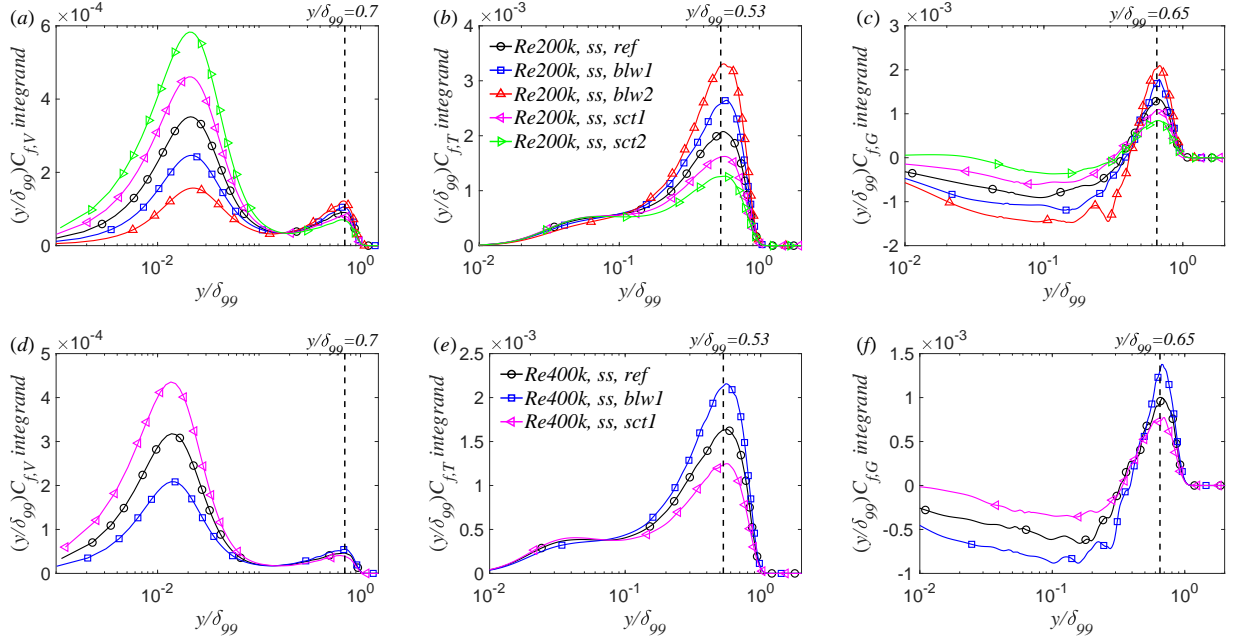


Figure 7: Pre-multiplied integrands of (a, d) $C_{f,v}$, (b, e) $C_{f,T}$, and (c, f) $C_{f,G}$, as a function of y/δ_{99} , on the suction side of a NACA4412 wing section at (a – c) $Re_c = 200,000$ and (d – f) $Re_c = 400,000$.

where $-\langle u'_s v'_s \rangle$ represents the Reynolds stress carried by small-scale structures, $-\langle u'_l v'_l \rangle$ represents the Reynolds stress associated with large-scale structures, and $-\langle u'_s v'_l \rangle$ and $-\langle u'_l v'_s \rangle$ denote the scale interactions from small-to large- and from large- to small-scale structures, respectively. Substituting these Reynolds-stress components into equation (6), the term of TKE production ($C_{f,T}$) can be further divided into four parts, *viz.*

$$C_{f,T,ss} = 2/U_e^3 \int_0^\infty \langle -u'_s v'_s \rangle^+ \frac{\partial \langle u \rangle^+}{\partial y^+} dy^+, \quad (10)$$

$$C_{f,T,sl} = 2/U_e^3 \int_0^\infty \langle -u'_s v'_l \rangle^+ \frac{\partial \langle u \rangle^+}{\partial y^+} dy^+, \quad (11)$$

$$C_{f,T,ls} = 2/U_e^3 \int_0^\infty \langle -u'_l v'_s \rangle^+ \frac{\partial \langle u \rangle^+}{\partial y^+} dy^+, \quad (12)$$

$$C_{f,T,ll} = 2/U_e^3 \int_0^\infty \langle -u'_l v'_l \rangle^+ \frac{\partial \langle u \rangle^+}{\partial y^+} dy^+. \quad (13)$$

Similar to the analysis in Sec. 3.2, we show the wall-normal distributions of the y^+ -pre-multiplied integrands in equations (10)–(13) in figure 10. For the reference case without control, the small-scale motions play important roles both in the inner and outer region, as two comparable peaks are respectively observed there, as seen in figure 10(a). This is different from the phenomenon in channel flows (Agostini and Leschziner, 2019) and ZPG-TBLs, since the APG strengthens the energy of small-scale structures in the outer region (Tanarro et al., 2020). Whereas the large-scale structures dominate the production of $C_{f,T}$ in the outer region, which is associated with the enhanced generation of large-scale motions in APG-TBLs (Lee and Sung, 2008; Harun et al., 2013; Vinuesa et al., 2018). When blowing is applied, the distributions of $C_{f,T,ss}$ -contribution and $C_{f,T,ll}$ -contribution in the outer region are shifted upwards, suggesting that the wall-normal mass flux enhances the outer fluctuations of both small- and large-scale structures. Comparison between $C_{f,T,ss}$ and $C_{f,T,ll}$ indicates that the blowing raises the relative importance of large scales with respect to the small ones. In addition, the

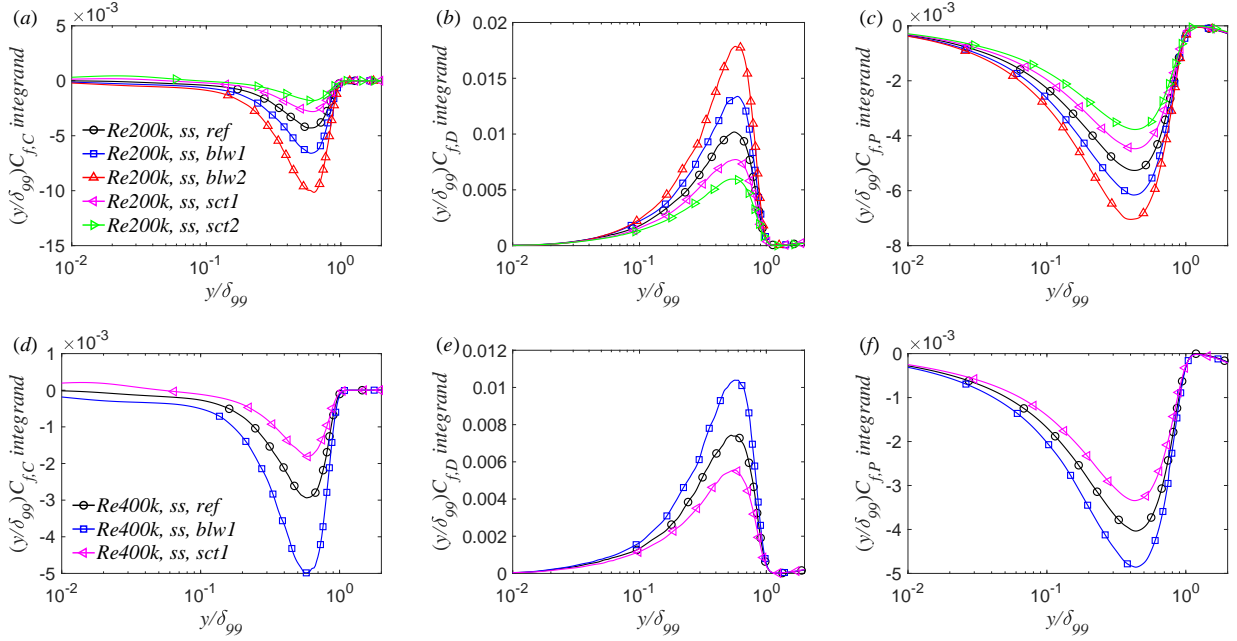


Figure 8: Pre-multiplied integrands of (a, d) $C_{f,C}$, (b, e) $C_{f,D}$, and (c, f) $C_{f,P}$, as a function of y/δ_{99} , on the suction side of a NACA4412 wing section at (a – c) $Re_c = 200,000$ and (d – f) $Re_c = 400,000$.

scale interactions ($C_{f,T,sl}$ and $C_{f,T,ls}$) mainly exhibited in the outer region are not very sensitive to the control schemes.

In order to further check the role of small- and large-scale motions in the generation of turbulence-kinetic-energy production, figure 11 quantifies their integrations normalized by $C_{f,T}$ itself. We can find that the blowing and suction have opposite influences on the contributions of small- and large-scale motions, that is, blowing is able to enhance the contribution of large-scales and to suppress the contribution of small-scales, whereas suction behaves contrarily. As for the scale-interactions, *i.e.* $C_{f,T,sl}$ and $C_{f,T,ls}$, they account for approximately 20% of the total $C_{f,T}$ and remain almost unchanged with different control strategies.

4 Friction-drag decomposition on the pressure side

In this section, we pay attention to the pressure side of a NACA4412 wing section, where the TBLs are subjected to favorable pressure gradients. Figure 12 shows the skin-friction coefficients on the pressure side of the airfoil. In spite of the favorable pressure gradients, blowing is still able to reduce the friction drag. Whereas, the skin-friction coefficients are no longer decreased monotonously with regard to x/c if compared with those on the suction side of the airfoil, which may be caused by the coupling influences of Re_τ and FPGs (Atzori et al., 2020). The relative errors ($[(C_{f,V} + C_{f,T} + C_{f,G} - C_f)/C_f]$) of the friction-drag decomposition are limited within $\pm 0.03\%$.

Key points of the decomposition results on the pressure side are listed below:

- The variations of $C_{f,V}$, $C_{f,T}$, and $C_{f,G}$ (see figures 13(a)–13(c)) are similar to the results on the suction side, that is, by blowing, $C_{f,V}$ and $C_{f,T}$ are decreased, and $C_{f,G}$ is reduced. As for the sub-constituents of $C_{f,G}$ in figures 13(d)–13(f), blowing reduces $C_{f,C}$, similar to the observations on the suction side; however, differently, blowing just increases $C_{f,D}$ until $x/c \approx 0.85$ and then decreases; in contrary to the control effects on the suction side, $C_{f,P}$ is increased, suggesting that blowing strengthens the FPG on the pressure side of NACA4412. Stronger intensity of blowing leads to larger increases or decreases of the constituents.

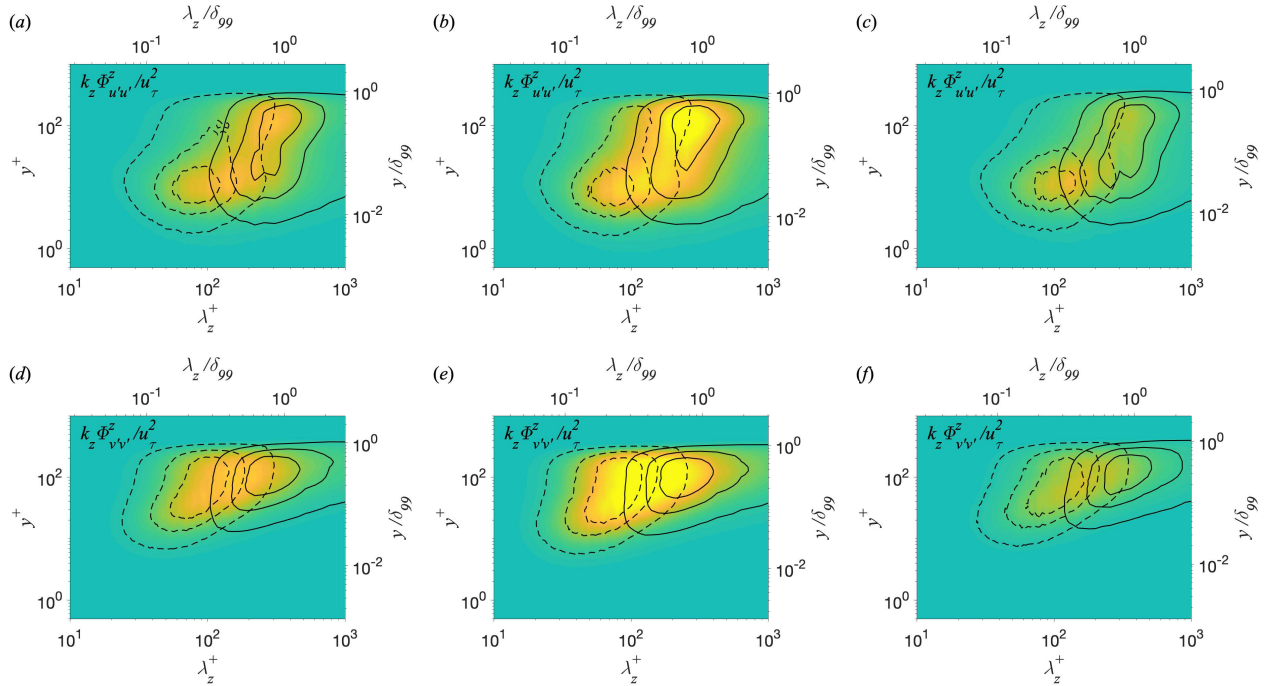


Figure 9: Spanwise pre-multiplied spectra of the tangential and normal velocity fluctuations on the suction side of a NACA4412 wing section at $Re_c = 400,000$ (a, c) without control, with (b, e) uniform blowing and (c, f) uniform suction. The nephogram represents the spectra of the full field; the dashed and solid contour lines represent those of small and large scales, respectively.

- Again, near-linear dependence of R_i on the intensity of blowing is still observed within the range of V_{wall}/U_∞ under scrutiny, as seen in figure 14.

- At $x/c \approx 0.75$ (similar features are observed at other positions), the wall-normal distributions of the C_f -constituents are plotted in figure 15. With the presence of FPG, the outer peak of $C_{f,V}$ is barely legible, and the outer peak of $C_{f,T}$ is comparable to the inner one, which are different from the results on the suction side. With blowing, the outer peak of $C_{f,T}$ is also increased however by a lesser amount, probably because that the FPG attenuates the outer-layer Reynolds shear stress and the production of turbulence kinetic energy (Harun et al., 2013). In figure 16, different from the observation in figure 8, the generation of $C_{f,C}$ mainly arises from the inner-layer dynamics on the pressure side of the airfoil.

- The peak locations in figures 15 and 16 are well collapsed when normalized by inner or outer units. It suggests that the self-similar features of turbulence statistics will not be affected by the presence of FPG. Note that the distributions in figures 15(a)-15(c) are not plotted as a function of y/δ_{99} since the friction Reynolds numbers of these three cases at $x/c \approx 0.75$ are very similar, being $Re_\tau \approx 177, 185,$ and 187 in the case of “*Re200k, ps, ref*”, “*Re200k, ps, blw1*”, and “*Re200k, ps, blw2*”, respectively.

- At last, EMD was not conducted, since the inner-outer scale separation is less evident in the FPG-TBLs at such low Re_τ than those on the suction side of the airfoil.

5 Conclusion

We employed the RD identity in conjunction with empirical mode decomposition (EMD) to study the control effects of uniform blowing and suction on the generation of mean friction drag on a NACA4412 airfoil at chord

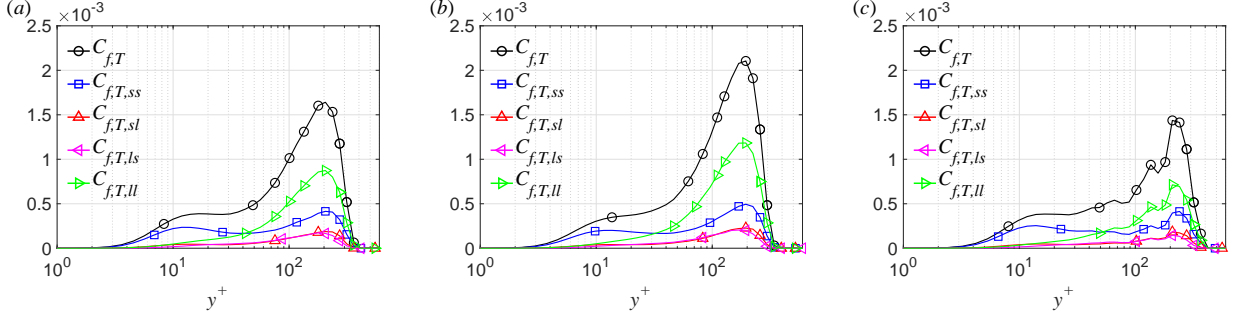


Figure 10: Pre-multiplied integrands of $C_{f,T,i}$ as a function of y^+ on the suction side of a NACA4412 wing section at $Re_c = 400,000$ (a) without control, with (b) uniform blowing and (c) uniform suction. Note that the premultiplication factor is y^+ .

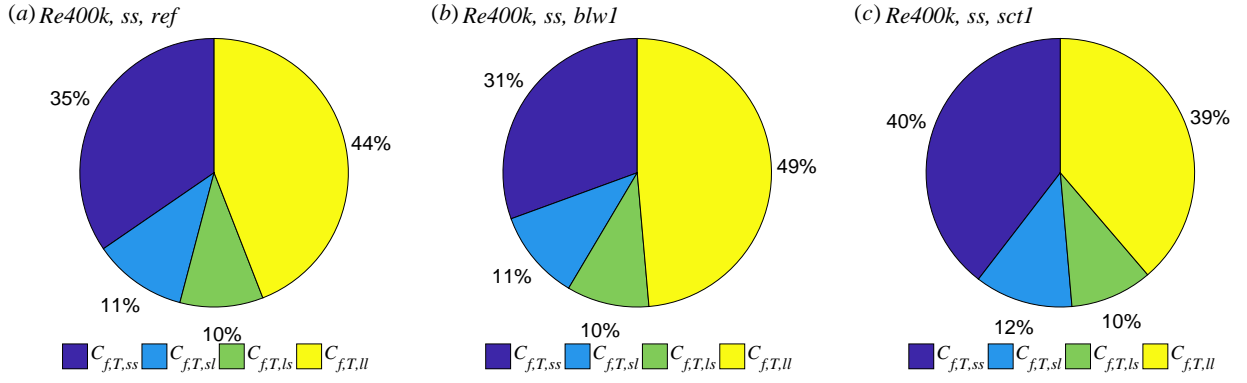


Figure 11: Scale-specific contributions ($C_{f,T,ss}$, $C_{f,T,sl}$, $C_{f,T,ls}$, and $C_{f,T,ll}$ normalized by $C_{f,T}$ itself) on the suction side of the NACA4412 wing section at $Re_c = 400,000$ (a) without control, with (b) uniform blowing and (c) uniform suction.

Reynolds numbers $Re_c=200,000$ and $400,000$. In general, blowing reduces the mean friction drag, and suction increases the friction drag, both on the suction and pressure sides of the airfoil. With the RD identity, the mean friction drag on the airfoil is decomposed into three components, associated with viscous dissipation ($C_{f,V}$), turbulence-kinetic-energy production ($C_{f,T}$), and spatial growth of the flow ($C_{f,G}$), respectively. The $C_{f,G}$ component is further decomposed into three terms related to the mean wall-normal convection ($C_{f,C}$), streamwise development ($C_{f,D}$), and the pressure gradient ($C_{f,P}$). The effects of suction on these C_f -constituents are quite opposite to those of blowing, thus we just summarize the key conclusions in the blowing cases.

For the adverse-pressure-gradient turbulent boundary layers on the suction side of the airfoil, concluding remarks are listed as below:

- Blowing reduces the generation of $C_{f,V}$ and $C_{f,G}$, while increases that of $C_{f,T}$. The drag reduction with blowing is mostly attributed to $C_{f,G}$, which results from the decreased $C_{f,C}$ and $C_{f,P}$, which overwhelm the increase in $C_{f,D}$. The integrated C_f -constituents over the control surface are observed to be linearly dependent on the intensity of blowing, and weakly influenced by the chord Reynolds number (at least within the parameters we considered).

- Wall-normal distributions of the C_f -constituents at $x/c \approx 0.75$ are checked to clarify how the control schemes impact the sources of friction-drag generation. With blowing, the generation of $C_{f,V}$, which is mainly related to the inner-layer dynamics, is suppressed in the inner region ($y^+ < 30$), while it is enhanced in the

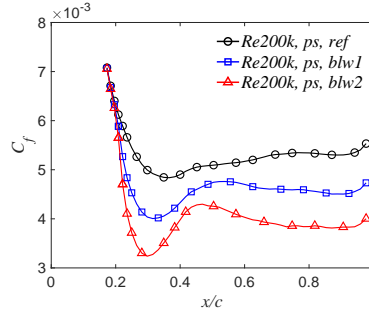


Figure 12: Variation of skin-friction coefficients on the pressure side of the NACA4412 wing section at $Re_c = 200,000$.

outer region. Contrarily, the generation of $C_{f,T}$, mainly originates from the outer-layer motions, is amplified by the blowing. These phenomena are linked to the variations of the wall-normal velocity gradients and Reynolds shear stresses in the wall-normal direction. The generation of $C_{f,G}$ results from a counterbalance between the negative work done by $C_{f,C}$ and $C_{f,P}$ and the positive work by $C_{f,D}$. Blowing is able to enhance the generation of all sub-components, as the strengthened adverse pressure gradient promotes a more pronounced growth of the boundary layer and a more prominent outer region (Vinuesa et al., 2018).

- We observed that, in the wall-normal direction, the inner-peak locations of $C_{f,V-}$ and $C_{f,T-}$ contributions scale well in the inner unit (δ_v), and the outer-peak locations of $C_{f,V-}$, $C_{f,T-}$, $C_{f,G-}$ as well as its sub-contributions, collapse well in the outer unit (δ_{99}), regardless of the friction Reynolds number, control scheme, and the intensity of blowing/suction. This reveals that self similarity is exhibited in inner or outer scales for the turbulence statistics associated with the friction-drag generation.

- The small- and large-scale structures are separated with empirical mode decomposition (EMD), aiming to analyze the scale-specific contribution of turbulent motions to friction-drag generation. Results unveil that, normalized by $C_{f,T}$ itself, blowing is able to enhance the contribution of large-scale motions and to suppress that of small scales; note that suction behaves contrarily. The contributions related to cross-scale interactions remain almost unchanged with different control strategies.

For the favorable-pressure-gradient turbulent boundary layers on the pressure side of the airfoil, the most significant observation is that the outer-layer motions are of less importance for the generation of C_f -constituents. In the case of blowing, the generation of $C_{f,P}$ is increased, which is the opposite behavior to that on the suction side of the airfoil.

Acknowledgments

The funding support of the National Natural Science Foundation of China (under the grant No. 91952302 and 92052101) is acknowledged. Davide Gatti acknowledges support by the state of Baden-Württemberg through bwHPC. Marco Atzori, Ricardo Vinuesa and Philipp Schlatter also acknowledge support from the Swedish Foundation for Strategic Research, project “In-Situ Big Data Analysis for Flow and Climate Simulations” (ref. number BD15-0082), from the Knut and Alice Wallenberg Foundation and from the Swedish Research Council (VR). The simulations were performed on resources provided by the Swedish National Infrastructure for Computing (SNIC) and within the project CWING on the national supercomputer Cray XC40 Hazel Hen at the High Performance Computing Center Stuttgart (HLRS).

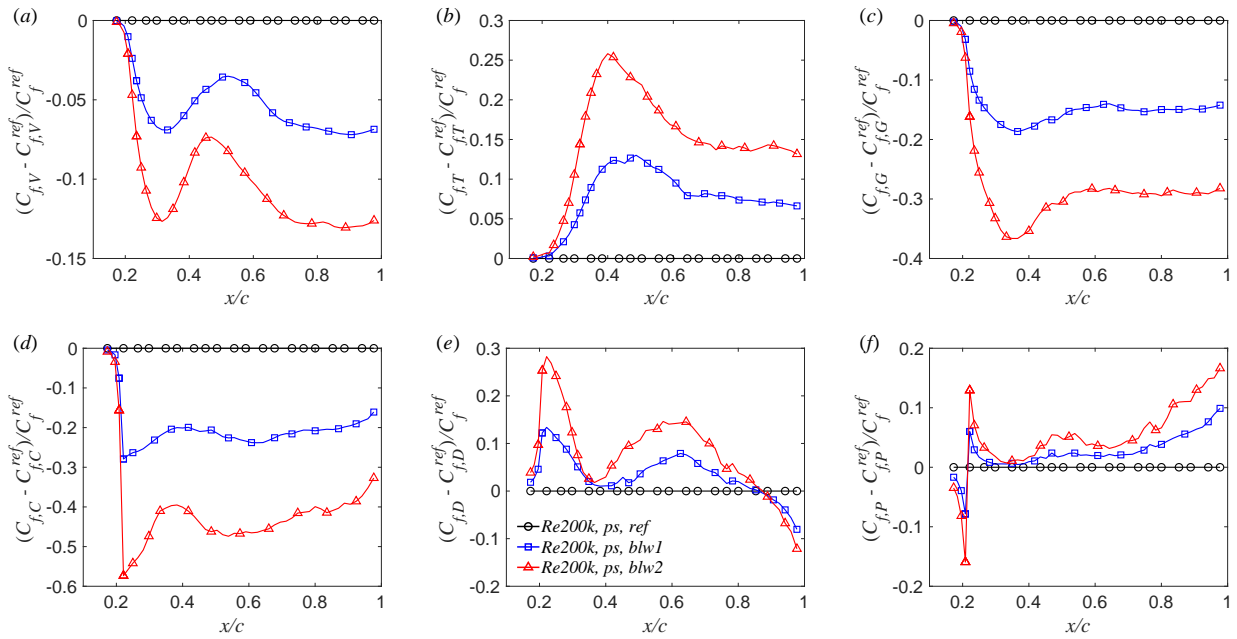


Figure 13: Variation of (a) $C_{f,V}$, (b) $C_{f,T}$, (c) $C_{f,G}$, (d) $C_{f,C}$, (e) $C_{f,D}$, and (f) $C_{f,P}$ with regard to the reference case on the pressure side of NACA4412 at $Re_c = 200,000$.

References

- L. Agostini and M. A. Leschziner. On the influence of outer large-scale structures on near-wall turbulence in channel flow. *Phys. Fluids*, 26(7):075107, 2014.
- L. Agostini and M. A. Leschziner. Predicting the response of small-scale near-wall turbulence to large-scale outer motions. *Phys. Fluids*, 28(1):015107, 2016.
- L. Agostini and M. A. Leschziner. The connection between the spectrum of turbulent scales and the skin-friction statistics in channel flow at $Re_\tau \approx 1000$. *J. Fluid Mech.*, 871:22–51, 2019.
- P. J. Ansell and M. J. Balajewicz. Separation of unsteady scales in a mixing layer using empirical mode decomposition. *AIAA J.*, 55(2):419–434, 2017.
- M. Atzori, R. Vinuesa, G. Fahland, A. Stroh, D. Gatti, B. Frohnapfel, and P. Schlatter. Aerodynamic effects of uniform blowing and suction on a NACA4412 airfoil. *Flow, Turbul. Combust.*, 105:735–759, 2020.
- A. Banner, É. Garnier, and P. Sagaut. Riblet flow model based on an extended FIK identity. *Flow, Turbul. Combust.*, 95(2-3):351–376, 2015.
- A. Bobke, R. Örlü, and P. Schlatter. Simulations of turbulent asymptotic suction boundary layers. *J. Turbul.*, 17(2):157–180, 2016.
- C. Cheng, W.-P. Li, A. Lozano-Durán, and H. Liu. Identity of attached eddies in turbulent channel flows with bidimensional empirical mode decomposition. *J. Fluid Mech.*, 870:1037–1071, 2019.
- F. H. Clauser. The turbulent boundary layer in adverse pressure gradients. *J. Aero. Sci.*, 21:91–108, 1954.
- F. H. Clauser. The turbulent boundary layer. *Adv. Appl. Mech.*, 4:1–51, 1956.
- S. Deck, N. Renard, R. Laraufie, and P. É. Weiss. Large-scale contribution to mean wall shear stress in high-Reynolds-number flat-plate boundary layers up to $Re_\theta = 13650$. *J. Fluid Mech.*, 743:202–248, 2014.
- E. Dogan, R. Örlü, D. Gatti, R. Vinuesa, and P. Schlatter. Quantification of amplitude modulation in wall-bounded turbulence. *Fluid Dyn. Res.*, 51:011408, 2019.
- K. Eto, Y. Kondo, K. Fukagata, and N. Tokugawa. Assessment of friction drag reduction on a Clark-Y airfoil

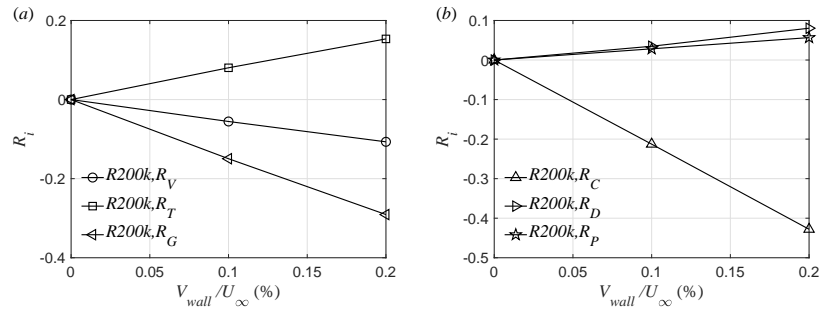


Figure 14: Total friction-drag change rate as a function of control intensity (V_{wall}/U_∞) on the pressure side of NACA4412.

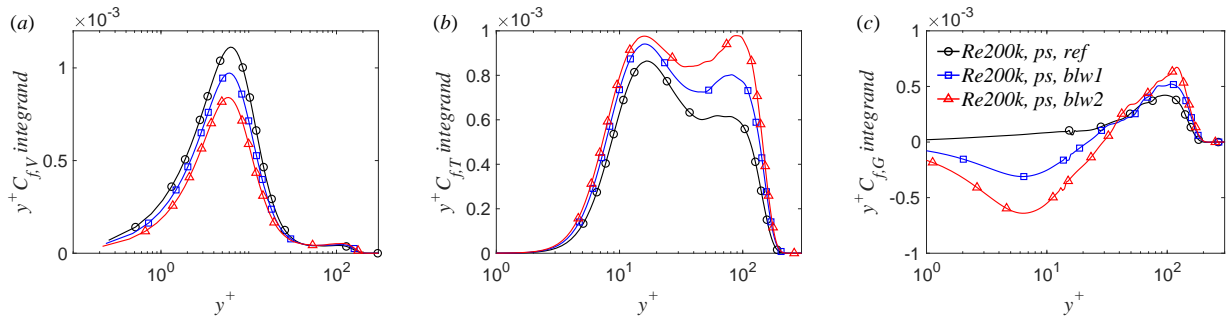


Figure 15: Pre-multiplied integrands of (a) $C_{f,V}$, (b) $C_{f,T}$, and (c) $C_{f,G}$, as a function of y^+ , on the pressure side of NACA4412 at $Re_c = 200,000$.

by uniform blowing. *AIAA J.*, 57(7):2774–2782, 2019.

G. Fahland, A. Stroh, B. Frohnäpfel, M. Atzori, R. Vinuesa, P. Schlatter, and D. Gatti. Investigation of blowing and suction for turbulent flow control on airfoils. *AIAA J.*, (To Appear), 03 2021.

Y.-T. Fan, C. Cheng, and W.-P. Li. Effects of the Reynolds number on the mean skin friction decomposition in turbulent channel flows. *Appl. Math. Mech. (English Ed.)*, 40(3):331–342, 2019a.

Y.-T. Fan, W.-P. Li, and S. Pirozzoli. Decomposition of the mean friction drag in zero-pressure-gradient turbulent boundary layers. *Phys. Fluids*, 31(8):086105, 2019b.

Y.-T. Fan, W.-P. Li, M. Atzori, R. Pozuelo, P. Schlatter, and R. Vinuesa. Decomposition of the mean friction drag in adverse-pressure-gradient turbulent boundary layers. *Phys. Rev. Fluids*, 5:114608, 2020a.

Y.-T. Fan, W.-P. Li, and S. Pirozzoli. Energy-based decomposition of friction drag in turbulent square-duct flows. *Int. J. Heat Fluid Flow*, 86:108731, 2020b. ISSN 0142-727X.

P. F. Fischer, J. W. Lottes, and S. G. Kerkemeier. Nek5000: Open source spectral element CFD solver. Available at: <http://nek5000.mcs.anl.gov>, 2008.

K. Fukagata, K. Iwamoto, and N. Kasagi. Contribution of reynolds stress distribution to the skin friction in wall-bounded flows. *Phys. Fluids*, 14(11):L73–L76, 2002.

M. Gad-el Hak. Interactive control of turbulent boundary layers - A futuristic overview. *AIAA J.*, 32(9):1753–1765, 1994.

Z. Harun, J. P. Monty, R. Mathis, and I. Marusic. Pressure gradient effects on the large-scale structure of turbulent boundary layers. *J. Fluid Mech.*, 715:477–498, 2013.

N. E. Huang, Z. Shen, S. R. Long, M. C. Wu, H. H. Shih, Q. Zheng, N.-C. Yen, C. C. Tung, and H. H. Liu. The empirical mode decomposition and the Hilbert spectrum for nonlinear and non-stationary time series analysis. *Proc. R. Soc. Lond. A*, 454:903–995, 1998.

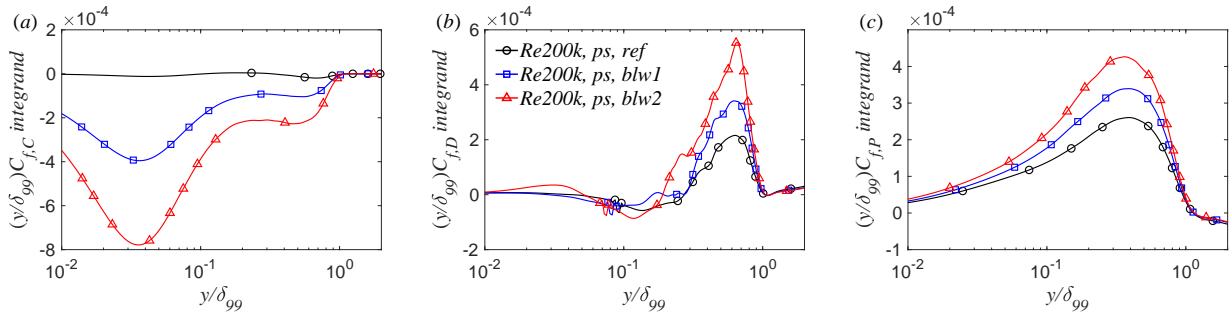


Figure 16: Pre-multiplied integrands of (a) $C_{f,C}$, (b) $C_{f,D}$, and (c) $C_{f,P}$, as a function of y/δ_{99} , on the pressure side of NACA4412 at $Re_c = 200,000$.

- Y. X. Huang, F. G. Schmitt, Z. M. Lu, and Y. L. Liu. An amplitude-frequency study of turbulent scaling intermittency using empirical mode decomposition and Hilbert spectral analysis. *Europhys. Lett.*, 84(4): 40010, nov 2008.
- D. Hwang. A proof of concept experiment for reducing skin friction by using a micro-blowing technique. *NASA*, pages TM-107315, 1996.
- D. Hwang. Review of research into the concept of the microblowing technique for turbulent skin friction reduction. *Prog. Aerosp. Sci.*, 40:559–575, 2004.
- Y. Kametani and K. Fukagata. Direct numerical simulation of spatially developing turbulent boundary layers with uniform blowing or suction. *J. Fluid Mech.*, 681:154–172, 2011.
- Y. Kametani, K. Fukagata, R. Örlü, and P. Schlatter. Effect of uniform blowing/suction in a turbulent boundary layer at moderate Reynolds number. *Int. J. Heat Fluid Flow*, 55:132–142, 2015.
- K. Kim, H.-J. Sung, and M.-K. Chung. Assessment of local blowing and suction in a turbulent boundary layer. *AIAA J.*, 40(1):175–177, 2002.
- V. I. Kornilov. Current state and prospects of researches on the control of turbulent boundary layer by air blowing. *Prog. Aerosp. Sci.*, 76:1–23, 2015.
- V. I. Kornilov. Implementation of air injection into the turbulent boundary layer of aircraft wing using external pressurized flow. *Thermophys. Aeromech.*, 24:175–185, 2017.
- V. I. Kornilov. Combined blowing/suction flow control on low-speed airfoils. *Flow Turbul. Combust.*, 106: 81–108, 2021.
- V. I. Kornilov, I. N. Kavun, and A. N. Popkov. Modification of turbulent airfoil section flow using a combined control action. *Thermophys. Aeromech.*, 26:165–178, 2019.
- J.-H. Lee and H.-J. Sung. Effects of an adverse pressure gradient on a turbulent boundary layer. *Int. J. Heat Fluid Flow*, 29(3):568–578, 2008.
- W.-P. Li. Turbulence statistics of flow over a drag-reducing and a drag-increasing riblet-mounted surface. *Aerosp. Sci. Technol.*, 104:106003, 2020. ISSN 1270-9638.
- W.-P. Li, Y.-T. Fan, D. Modesti, and C. Cheng. Decomposition of the mean skin-friction drag in compressible turbulent channel flows. *J. Fluid Mech.*, 875:101–123, 2019.
- J. L. Lumley. The structure of inhomogeneous turbulent flows. In A. M. Yaglom and V. I. Tartarsky, editors, *Atmospheric Turbulence and Radio Wave Propagation*, pages 166–177. 1967.
- O. A. Mahfoze, A. Moody, A. Wynn, R. D. Whalley, and S. Laizet. Reducing the skin-friction drag of a turbulent boundary-layer flow with low-amplitude wall-normal blowing within a Bayesian optimization framework. *Phys. Rev. Fluids*, 4:094601, 2019.
- F. Mehdi and C. M. White. Integral form of the skin friction coefficient suitable for experimental data. *Exp. Fluids*, 50(1):43–51, 2011.

- F. Mehdi, T. G. Johansson, C. M. White, and J. W. Naughton. On determining wall shear stress in spatially developing two-dimensional wall-bounded flows. *Exp. Fluids*, 55(1):1656, 2014.
- D. Modesti, S. Pirozzoli, P. Orlandi, and F. Grasso. On the role of secondary motions in turbulent square duct flow. *J. Fluid Mech.*, 847:R1, 2018. doi: 10.1017/jfm.2018.391.
- J. Park and H. Choi. Effects of uniform blowing or suction from a spanwise slot on a turbulent boundary layer flow. *Phys. Fluids*, 11(10):3095–3105, 1999.
- A. T. Patera. A spectral element method for fluid dynamics: laminar flow in a channel expansion. *J. Comput. Phys.*, 54:468–488, 1984.
- Y. Peet and P. Sagaut. Theoretical prediction of turbulent skin friction on geometrically complex surfaces. *Phys. Fluids*, 21(10):105105, 2009.
- W. Ran, A. Zare, and M. R. Jovanović. Model-based design of riblets for turbulent drag reduction. *J. Fluid Mech.*, 906:A7, 2021. doi: 10.1017/jfm.2020.722.
- A. Rastegari and R. Akhavan. On the mechanism of turbulent drag reduction with super-hydrophobic surfaces. *J. Fluid Mech.*, 773:R4, 2015. doi: 10.1017/jfm.2015.266.
- N. Renard and S. Deck. A theoretical decomposition of mean skin friction generation into physical phenomena across the boundary layer. *J. Fluid Mech.*, 790:339–367, 2016.
- J. C. Rotta. Über die theorie der turbulenten grenzschichten. *Mitt. Max Planck Inst. Strömungsforsch., Göttingen*, 1950.
- C. Sanmiguel Vila, R. Vinuesa, S. Discetti, A. Ianiro, P. Schlatter, and R. Örlü. Separating adverse-pressure-gradient and Reynolds-number effects in turbulent boundary layers. *Phys. Rev. Fluids*, 5:064609, 2020.
- P. Schlatter and R. Örlü. Turbulent boundary layers at moderate Reynolds numbers: inflow length and tripping effects. *J. Fluid Mech.*, 710:5–34, 2012.
- A. Stroh, B. Frohnäpfel, P. Schlatter, and Y. Hasegawa. A comparison of opposition control in turbulent boundary layer and turbulent channel flow. *Phys. Fluids*, 27:075101, 2015.
- A. Stroh, Y. Hasegawa, P. Schlatter, and B. Frohnäpfel. Global effect of local skin friction drag reduction in spatially developing turbulent boundary layer. *J. Fluid Mech.*, 805:303–321, 2016. doi: 10.1017/jfm.2016.545.
- Á. Tanarro, R. Vinuesa, and P. Schlatter. Effect of adverse pressure gradients on turbulent wing boundary layers. *J. Fluid Mech.*, 883:A8, 2020.
- E. Toubert and M. A. Leschziner. Near-wall streak modification by spanwise oscillatory wall motion and drag-reduction mechanisms. *J. Fluid Mech.*, 693:150–200, 2012. doi: 10.1017/jfm.2011.507.
- R. Vinuesa and P. Schlatter. Skin-friction control of the flow around a wing section through uniform blowing. In *Proceedings of European Drag Reduction and Flow Control Meeting (EDRFCM)*, 2017.
- R. Vinuesa, P. S. Negi, M. Atzori, A. Hanifi, D. S. Henningson, and P. Schlatter. Turbulent boundary layers around wing sections up to $Re_c=1,000,000$. *Int. J. Heat Fluid Flow*, 72:86 – 99, 2018.
- W.-K. Wang, C. Pan, and J.-J. Wang. Quasi-bivariate variational mode decomposition as a tool of scale analysis in wall-bounded turbulence. *Exp. Fluids*, 59:1, 2018.
- W.-K. Wang, C. Pan, and J.-J. Wang. Multi-component variational mode decomposition and its application on wall-bounded turbulence. *Exp. Fluids*, 60:95, 2019.
- T. Wei. Integral properties of turbulent-kinetic-energy production and dissipation in turbulent wall-bounded flows. *J. Fluid Mech.*, 854:449–473, 2018.
- G. Welch, L. Larosiliere, D. Hwang, and J. Wood. *Effectiveness of micro-blowing technique in adverse pressure gradients*. 2001.
- C. M. White and M. G. Mungal. Mechanics and prediction of turbulent drag reduction with polymer additives. *Annu. Rev. Fluid Mech.*, 40(1):235–256, 2008.
- Y. Wu and K. T. Christensen. Spatial structure of a turbulent boundary layer with irregular surface roughness. *J. Fluid Mech.*, 655:380–418, 2010.

- M. Yoon, J. Ahn, J. Hwang, and H. J. Sung. Contribution of velocity-vorticity correlations to the frictional drag in wall-bounded turbulent flows. *Phys. Fluids*, 28(8):081702, 2016.
- M. Yoon, J. Hwang, and H. J. Sung. Contribution of large-scale motions to the skin friction in a moderate adverse pressure gradient turbulent boundary layer. *J. Fluid Mech.*, 848:288–311, 2018.